Received: 29 June 2023 | Revised: 11 October 2023 | Accepted: 15 October 2023

DOI: 10.1002/pro.4810

RESEARCH ARTICLE

THE PROTEIN SOCIETY WILEY

Interaction between huntingtin exon 1 and HEAT repeat structure probed by chimeric model proteins

Hong Zhang[1,2,3] | **Si Wu**[1,2] | **Laura S. Itzhaki**[4] | **Sarah Perrett**[1,2]

[1]National Laboratory of Biomacromolecules, CAS Center for Excellence in Biomacromolecules, Institute of Biophysics, Chinese Academy of Sciences, Beijing, China

[2]University of the Chinese Academy of Sciences, Beijing, China

[3]Institute of Basic Medical Sciences, Chinese Academy of Medical Sciences, Peking Union Medical College, Beijing, China

[4]Department of Pharmacology, University of Cambridge, Cambridge, UK

Correspondence
Hong Zhang and Sarah Perrett, National Laboratory of Biomacromolecules, Institute of Biophysics, Chinese Academy of Sciences, 15 Datun Road, Chaoyang District, Beijing 100101, China.
Email: zhanghong@ibms.pumc.edu.cn; sarah.perrett@cantab.net

Funding information
National Natural Science Foundation of China, Grant/Award Numbers: 31920103011, 31770829, 32171443; National Laboratory of Biomacromolecules; CAS Center of Excellence in Biomacromolecules

Review Editor: Aitziber L. Cortajarena

Abstract

Huntington disease (HD) is associated with aggregation of huntingtin (HTT) protein containing over 35 continuous Q residues within the N-terminal exon 1 encoded region. The C-terminal of the HTT protein consists mainly of HEAT repeat structure which serves as a scaffold for multiple cellular activities. Structural and biochemical analysis of the intact HTT protein has been hampered by its huge size (~300 kDa) and most in vitro studies to date have focused on the properties of the exon 1 region. To explore the interaction between HTT exon 1 and the HEAT repeat structure, we constructed chimeric proteins containing the N-terminal HTT exon 1 region and the HEAT repeat protein PR65/A. The results indicate that HTT exon 1 slightly destabilizes the downstream HEAT repeat structure and endows the HEAT repeat structure with more conformational flexibility. Wild-type and pathological lengths of polyQ did not show differences in the interaction between HTT exon 1 and the HEAT repeats. With the C-terminal fusion of PR65/A, HTT exon 1 containing pathological lengths of polyQ could still form amyloid fibrils, but the higher-order architecture of fibrils and kinetics of fibril formation were affected by the C-terminal fusion of HEAT repeats. This indicates that interaction between HTT exon 1 and HEAT repeat structure is compatible with both normal function of HTT protein and the pathogenesis of HD, and this study provides a potential model for further exploration.

KEYWORDS
amyloid, HEAT repeat, huntingtin exon 1, polyQ, protein folding

1 | INTRODUCTION

Huntington disease (HD) is a dominantly autosomal inherited neurodegenerative disease, characterized by progressive movement disorders such as chorea, as well as cognitive impairment and psychiatric symptoms due to atrophy of the basal ganglia (primarily, striatum) and the cerebral cortex (Roze et al., 2010). Expansion of the CAG repeats over 35 in exon 1 of the huntingtin (*HTT*) gene is associated with the development of HD (The Huntington's Disease Collaborative Research Group, 1993). CAG expansion is related with at least 10 types of inherited diseases, and a common feature of these diseases is the amyloid fibril formation of the corresponding

Abbreviations: AFM, atomic force microscopy; CSM, center of spectral mass; HD, Huntington disease; HTT, huntingtin; polyQ, polyglutamine; PP2A, protein phosphatase 2A; PR65/A, the 65-kDa scaffolding A subunit of PP2A; SEC, size-exclusion chromatography; ThT, thioflavin T.

polyglutamine (polyQ) containing proteins (Gatchel and Zoghbi, 2005). HTT protein and its mutants (mutant huntingtin, mHTT) are ubiquitously expressed both at tissue and subcellular levels, with slightly higher expression levels in brain tissues, particularly in striatal neurons (Marques Sousa and Humbert, 2013). The functions of HTT in developing and mature organisms are numerous, corresponding to the output at the molecular level: (1) trafficking vesicles; (2) coordinating cell division; (3) regulating ciliogenesis; (4) mediating endocytosis, vesicle recycling, and endosomal trafficking; (5) involvement in autophagy; (6) regulating transcription (Saudou and Humbert, 2016). The multiple functions of HTT are attributed to multiple interactions with other proteins, and more than 350 HTT-interacting proteins have been identified and the corresponding HTT domains involved in the interaction have also been speculated (Harjes and Wanker, 2003; Culver et al., 2012).

The structural basis for the interaction of HTT with numerous partners is still not fully known. HTT is a 347-kDa protein with no sequence homology to any other known proteins. The HTT gene contains 67 exons and the exon 1 (coding 1–90 aa of HTT with 23 Q) accommodates an expansion-prone CAG stretch encoding for a polyQ segment (Caterino et al., 2018). The exon 1 contains a N-terminal highly conserved 17-residue nuclear export sequence named N17, the polyQ sequence and a downstream ~40 residue proline-rich domain occurring exclusively in mammals (Caterino et al., 2018). After the exon 1-encoded stretch, HTT features HEAT/HEAT-like motifs and helix-turn-helix repeats that are important in protein–protein recognition / interaction, suggesting that HTT works as a large scaffold for supramolecular assemblies (Caterino et al., 2018). The HEAT repeat motif is named after the first identified four HEAT-repeat proteins: **H**TT, **e**longation factor 3 (**E**F3), the 65-kDa scaffolding **A** subunit (PR65/**A**) of protein phosphatase 2A (PP2A) and the yeast kinase **T**OR1 (Andrade and Bork, 1995). HEAT repeat sequences can form an α-ROD structure which involves the stacking of repeats including two alpha helices packed together (Bourne et al., 2009).

When HTT is purified alone it forms oligomers and tends to aggregate, but the HTT–HAP40 complex is more conformationally homogeneous than HTT alone (Guo et al., 2018; Harding et al., 2019). The cryo-electron microscopy structure of the HTT–HAP40 complex shows that HTT consists of three domains in addition to the undetectable highly flexible N terminal exon 1, namely N- and C-terminal domains containing multiple HEAT repeats (N-HEAT and C-HEAT) linked by a smaller bridge domain. N-HEAT (residues 91–1684) forms a typical α-solenoid, comprising 21 HEAT repeats arranged as a one-and-a-half-turn right-handed superhelix, and C-HEAT (residues 2092–3098) comprises 12 HEAT repeats forming an elliptical ring (Guo et al., 2018). Multiple protease cleavage sites and post-translational modification (PTM) sites have been identified throughout HTT, and complex protease cleavages and PTMs were found to finely tune the function of HTT (Saudou and Humbert, 2016; Yalinca et al., 2019).

The HEAT repeats are relatively conserved in HTT and correspond to the core functions of HTT, while the HTT exon 1 is only poorly conserved, suggesting it has a role in fine modulation of the function of HTT with evolution (Saudou and Humbert, 2016). HTT exon 1 contributes to PTM regulation of HTT including ubiquitination, SUMOylation and phosphorylation, interaction of HTT with membranes, regulation of HTT interactions with its partners and the clearance and subcellular localization of HTT (Saudou and Humbert, 2016; Tao et al., 2019). The polyQ tract can participate in transcriptional regulation similar to transcription factors that include such motifs (Perutz et al., 1994). In vitro experiments revealed that free HTT exon 1 bearing Q of over 35 residues have increased tendency to form amyloid fibrils with the increasing number of Q (Scherzinger et al., 1997). In vivo experiments showed that HTT exon 1 is an essential component of aggregates in HD models (Hackam et al., 1998; Li and Li, 1998; Yang et al., 2020).

Interaction between HTT exon 1 and the downstream HEAT repeats may also be involved in HTT function and mechanism of HTT aggregation in vivo. The polyQ stretch can regulate HTT binding to its interacting proteins (Harjes and Wanker, 2003). However, the relationship between the two parts of HTT still remains unclear due to the difficulty of carrying out detailed studies on the intact protein. Research employing model proteins instead of HTT can also provide useful insight since purified HTT alone is heterogeneous and tends to aggregate. Glutathione S-transferase (GST) fusion exon 1 is commonly used for in vitro study of HTT fibril formation (Scherzinger et al., 1997; Muchowski et al., 2000; Wacker et al., 2004). However, GST fusion exon 1 constructs are not appropriate candidates for domain interaction research because they lack HEAT repeats, but instead contain dimer-forming GST. PR65/A is a 65-kDa HEAT repeat protein which contains 15 HEAT repeats forming an extended and curved structure like a hook (Figure 1a), and is the scaffolding subunit A of PP2A holoenzyme (Groves et al., 1999). Diverse functions of PP2A are mediated by combination of PR65/A with a number of different regulatory B subunits and the catalytic C subunit (Lechward et al., 2001). The accommodation of PR65/A with different regulatory B subunits is achieved through conformation flexibility of PR65/A upon binding of different ligands (Lechward et al., 2001). Unfolding of

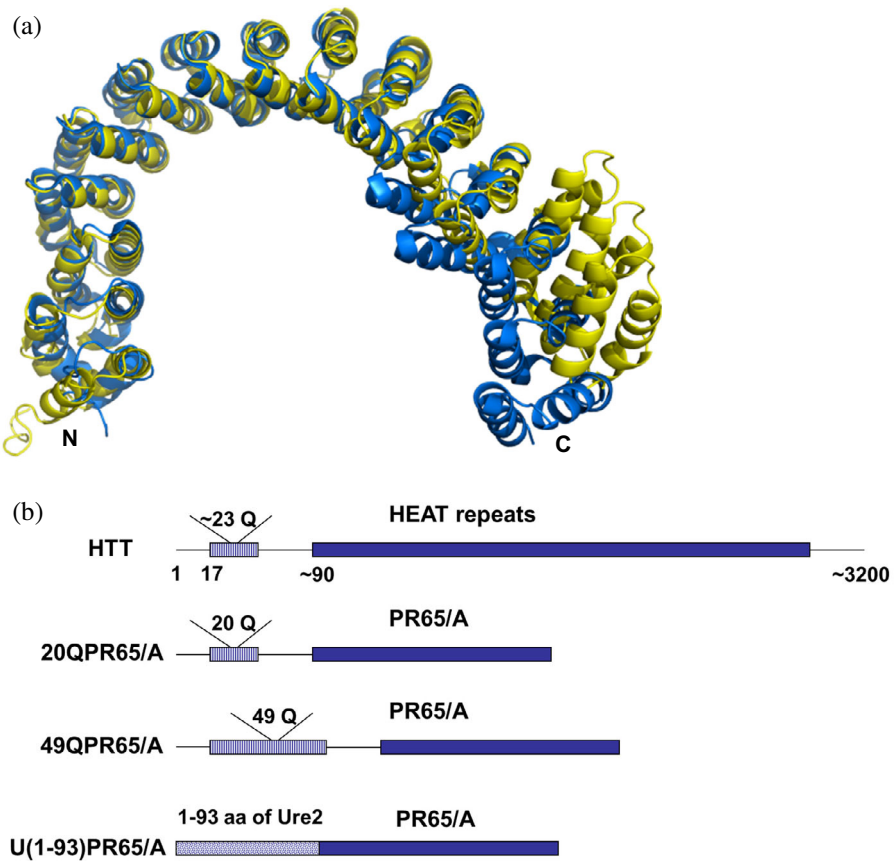

FIGURE 1 Structure of PR65/A and schematic diagram of chimeric proteins used in this study. (a) Crystal structure of PR65/A in apo form (PDB code 1B3U) shown in yellow and structure of PR65/A in ligand binding form (PDB code 2PF4) shown in blue. (b) Schematic diagram of chimeric proteins (20QPR65/A, 49QPR65/A and U(1-93)PR65/A) used in this study is shown; the extra linker between HTT exon 1 / Ure2 PrD and PR65/A is "LE". Full-length Huntingtin protein (HTT) which is composed of the N-terminal approximately 90 amino acids corresponding to polyQ-containing exon 1 region followed by the C-terminal HEAT repeats region.

PR65/A has been thoroughly studied and it has been shown that the noncontiguous folding / unfolding and the intrinsic dynamics of the HEAT repeat array orchestrates the assembly and activity of PP2A (Tsytlonok et al., 2013; Kaynak et al., 2023). Although HTT and PR65/A share little similarity in amino acid sequence, number of HEAT repeats, or higher order architecture, these proteins contain similar HEAT repeat structural units. Unlike the well-characterized structure of PR65/A (Groves et al., 1999; Tsytlonok et al., 2013), the HEAT repeats in HTT still lack clear characterization. Therefore, in this study we constructed PR65/A chimeric proteins with N-terminal fusion of HTT exon 1 containing 20 Q or 49 Q (20QPR65/A and 49QPR65/A, shown in Figure 1b) to mimic HTT and studied interaction between HTT exon 1 and the HEAT repeat structure. We tested the effect of N-terminal fusion of HTT exon 1 on HEAT repeat structure and conversely, the effect of HEAT repeat structure on amyloid fibril formation of HTT exon 1. We found that N-terminal fusion of HTT exon 1 destabilizes the PR65/A structure and increases conformation flexibility of PR65/A. Our results also indicate that HTT exon 1 bearing Q of over 35 residues can form amyloid fibrils with a HEAT repeat tail. However, the HEAT repeat tail retards HTT exon 1 fibril formation and affects the morphology of fibrils. These results suggest that HTT exon 1 interacts with the HEAT repeat structure in HTT, and so this interaction may contribute to the functional regulation of HTT and the pathogenesis or prevention of HD.

2 | RESULTS

2.1 | N-terminal fusion of HTT exon 1 perturbs the structure of PR65/A

HTT exon 1 in the non-fibrillar state is highly flexible and is not visible in the EM structure of HTT (Guo et al., 2018), although it tends to form some local structure (Saudou and Humbert, 2016; Caterino et al., 2018). In this study, HTT exon 1 containing either 20 Q or 49 Q was fused in front of PR65/A to investigate the interaction between HTT exon 1 with the HEAT repeat structure (Figure 1b). As a control, the highly flexible prion domain (PrD) of the yeast prion protein Ure2, which is of the same length as HTT exon 1 containing 23 Q and is also capable of driving amyloid formation (Jiang et al., 2004), was likewise fused to the N-terminal of PR65/A, to form the construct U(1-93)PR65/A (Figure 1b). The expression level and purification efficiency of 20QPR65/A and 49QPR65/A was much lower

than for PR65/A or U(1-93)PR65/A, suggesting that N-terminal fusion of HTT exon 1, but not N-terminal fusion of the Ure2 prion domain, decreases expression and may lead to aggregation of the chimeric proteins, although the two fibrillation-determining domains have some similar characteristics (i.e., sequence length, flexible structure and tendency to form amyloid fibrils).

Size exclusion chromatography (SEC) analysis of the four proteins indicated that there were no large aggregates present in the purified proteins and one kind of oligomeric state was predominant for each protein (Figure 2a). The molecular weight of the four proteins was further estimated from SEC analysis profiles and sedimentation equilibrium analysis as shown in Table 1. The calculated molecular weight of PR65/A and U(1-93)PR65/A were close to their theoretical values for monomer (Table 1), which is consistent with the reported monomeric state of PR65/A (Groves et al., 1999). However, the calculated molecular weight of 20QPR65/A and 49QPR65/A was about 50% larger than the expected value of monomer (Table 1). This suggests that 20QPR65/A and 49QPR65/A remain monomeric like PR65/A and U(1-93)PR65/A, but show a larger apparent size due to a larger hydrodynamic volume i.e. looser structure.

PR65/A contains five tryptophan residues (W140, W257, W417, W450 and W477), while HTT exon 1 and the Ure2 prion domain do not contain any tryptophan residues. Therefore, we can use the intrinsic fluorescence spectra to monitor structural changes in PR65/A upon N-terminal fusion. We found that the spectra of the four proteins fell into two distinct groups, and, compared with PR65/A and U(1-93)PR65/A, the maximum emission wavelength for 20QPR65/A and 49QPR65/A was blue shifted by 1–2 nm, and the calculated CSM (center of spectral mass—an indication of the local environment/solvent accessibility of the tryptophan residues in the protein) of intrinsic fluorescence spectra also showed similar trends (Figures 2b and 5b). PR65/A is an α-helix rich protein and shows typical characteristics of α-helical structure in its far-UV CD spectrum i.e. double minima and a strong signal at 222 nm (Figure 2c). It has been reported that HTT exon 1 shows a very weak signal in its far-UV CD spectrum indicating random coil in neutral buffers (Masino et al., 2002) as for the Ure2 PrD (Perrett and Jones, 2008). Therefore, the CD signals of PR65/A chimeras mainly reflect structure of PR65/A. The CD spectra of the four proteins also fell into two distinct groups. U(1-93)PR65/A had a similar CD spectrum to PR65/A, whereas those of 20QPR65/A and 49QPR65/A were similar but showed a smaller signal at 222 nm (Figure 2c). The fluorescence and CD results both suggest that HTT

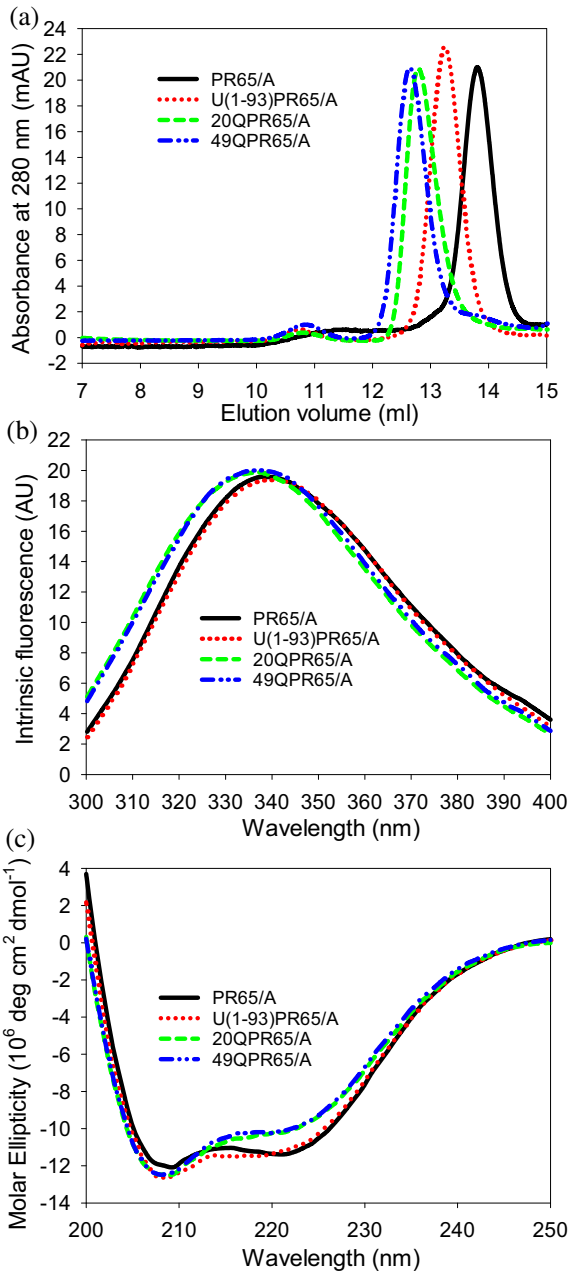

FIGURE 2 N-terminal fusion of HTT exon 1 perturbs the structure of PR65/A. (a) SEC analysis of PR65/A, U(1-93)PR65/A, 20QPR65/A and 49QPR65/A were performed in Buffer A (50 mM Tris–HCl buffer, pH 7.5, containing 150 mM NaCl and 2 mM DTT). Proteins of 10 μM were loaded onto a 24-ml Superdex 200 10/300 GL column. (b) Intrinsic fluorescence spectra (excited at 280 nm) of PR65/A, U(1-93)PR65/A, 20QPR65/A and 49QPR65/A of 0.4 μM were measured in Buffer B (50 mM MES buffer, pH 6.5, containing 2 mM DTT). (c) Far-UV CD spectra of PR65/A, U(1-93)PR65/A, 20QPR65/A and 49QPR65/A of 1 μM were measured in Buffer A. In (b) and (c) the curves were smoothed using the SigmaPlot software. Three independent replicates gave similar results and one typical data set is shown.

TABLE 1 Oligomeric state of native PR65/A, U(1-93)PR65/A, 20QPR65/A and 49QPR65/A determined by SEC and sedimentation equilibrium analysis.

	Actual molecular weight of monomer (kDa)	Buffer conditions	Calculated molecular weight (kDa)		Oligomeric state
			SEC	Sedimentation equilibrium	
PR65/A	65.4	Tris 7.5 buffer[a]	63.7	N/A	Monomer
		MES 6.5 buffer[b]	70.0	N/A	Monomer
U(1-93) PR65/A	75.8	Tris 7.5 buffer[a]	88.6	N/A	Monomer
		MES 6.5 buffer[b]	88.5	N/A	Monomer
20QPR65/A	75.3	Tris 7.5 buffer[a]	117.0	74.3	Monomer
		MES 6.5 buffer[b]	105.5	106.5	Monomer
49QPR65/A	79.1	Tris 7.5 buffer[a]	127.1	113.6	Monomer
		MES 6.5 buffer[b]	117.6	115.3	Monomer

[a]Tris 7.5 buffer: 50 mM Tris–HCl buffer, pH 7.5, containing 150 mM NaCl and 1 mM DTT (sedimentation equilibrium) or 2 mM DTT (SEC).
[b]MES 6.5 buffer: 50 mM MES buffer, pH 6.5, containing 1 mM DTT (sedimentation equilibrium) or 2 mM DTT (SEC).

exon 1, unlike the Ure2 PrD, disrupts the α-helical structure of PR65/A to some extent, probably by interaction between HTT exon 1 and the HEAT repeat structure, and there is no significant difference between 20 Q HTT exon 1 and 49 Q HTT exon 1 in the size of the effect.

2.2 | N-terminal fusion of HTT exon 1 increases the conformational flexibility of PR65/A

Although we observed differences in the intrinsic fluorescence spectra of PR65/A, U(1-93)PR65/A, 20QPR65/A and 49QPR65/A in Buffer B (50 mM MES buffer, pH 6.5, containing 2 mM DTT) (Figure 2b), we found that the intrinsic fluorescence spectra of PR65/A, U(1-93)PR65/A, 20QPR65/A and 49QPR65/A in Buffer A (50 mM Tris–HCl buffer, pH 7.5, containing 150 mM NaCl and 2 mM DTT) were similar (Figure 3a). Considering the difference in pH and salt concentration between the two buffers, we next measured the intrinsic fluorescence spectra of the four proteins in 50 mM MES buffer (pH 6.5) or 50 mM Tris–HCl buffer (pH 7.5), each containing 2 mM DTT and 0–200 mM NaCl. We found that the CSM values of the intrinsic fluorescence spectra of 20QPR65/A and 49QPR65/A were more sensitive to salt concentration than those of PR65/A and U(1-93)PR65/A (Figure 3b,c); for 20QPR65/A and 49QPR65/A, the CSM showed a clear red shift with increasing salt concentration and at higher concentrations of salt the CSM of 20QPR65/A and 49QPR65/A was closer to that of PR65/A and U(1-93) PR65/A (Figure 3b,c). These results suggest that the conformational stability of 20QPR65/A and 49QPR65/A is more sensitive to salt than PR65/A and U(1-93)PR65/A, and salt appears to stabilize the structure of 20QPR65/A and 49QPR65/A for reasons that are not entirely clear, but may involve electrostatic shielding and disruption of hydrogen bonds or polar interactions that are unfavorable to stability of the HTT-exon 1-fusion proteins.

ANS (8-anilino-1-naphthalenesulfonic acid) is a hydrophobic probe that is commonly used to indicate the degree of hydrophobicity on the surface of proteins and formation of partially folded states. The crystal structure of PR65/A indicates that there are some hydrophobic patches on its surface that are important for the interactions of PR65/A with its binding partners (Groves et al., 1999). It was surprising to find that 20QPR65/A and 49QPR65/A had much higher ANS fluorescence intensity than PR65/A and U(1-93)PR65/A (Figure 4a), suggesting that 20QPR65/A and 49QPR65/A have more hydrophobic surfaces than PR65/A and U(1-93)PR65/A. The ANS binding properties of the four proteins were further compared by measuring the ANS binding at different ANS to protein ratios. We found that ANS binding to PR65/A reached a maximum at a very high ANS:protein ratio (about 1500, much higher than most proteins) and after that the ANS binding decreased (Figure 4b,c). The paradoxical decrease in ANS fluorescence at higher ANS concentration suggests a reduction in the number of binding sites that are accessible and bound, indicating that ANS binding induces a conformational change in the HEAT repeat structure of PR65/A. ANS at low concentrations may lead to more exposure of hydrophobic surface allowing increased ANS binding until the structure of PR65/A is disrupted by ANS binding, and the disrupted PR65/A structure then binds fewer molecules of ANS. The ANS:protein ratio at maximum fluorescence intensity for 20QPR65/A and 49QPR65/A was much

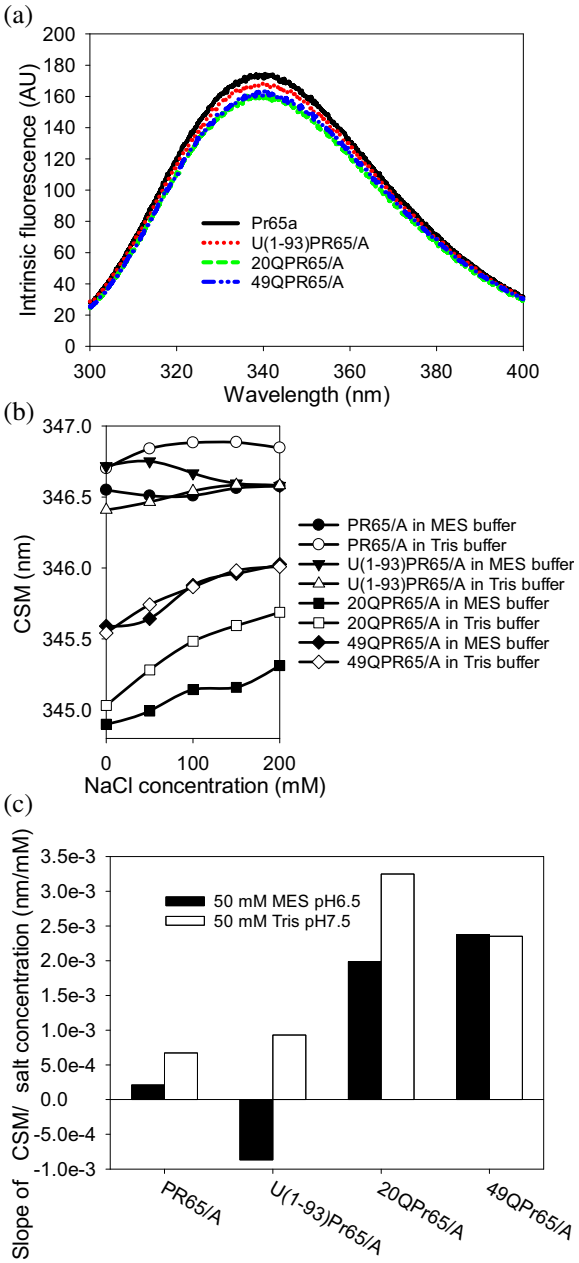

FIGURE 3 N-terminal fusion of HTT exon 1 increases the conformational flexibility of PR65/A in a salt-concentration dependent manner. (a) Intrinsic fluorescence spectra (excited at 280 nm) of 0.4 μM PR65/A, U(1-93)PR65/A, 20QPR65/A and 49QPR65/A were compared in Buffer A (50 mM Tris–HCl buffer, pH 7.5, containing 150 mM NaCl and 2 mM DTT). (b) Center of spectral mass (CSM) of intrinsic fluorescence spectra of 0.4 μM PR65/A, U(1-93)PR65/A, 20QPR65/A and 49QPR65/A in 50 mM Tris–HCl buffer, pH 7.5, or 50 mM MES buffer, pH 6.5, containing 2 mM DTT and different concentrations of NaCl, were measured as indicated. (c) Slopes of CSM against salt concentration for PR65/A, U(1-93)PR65/A, 20QPR65/A and 49QPR65/A in 50 mM Tris–HCl buffer, pH 7.5, or 50 mM MES buffer, pH 6.5, containing 2 mM DTT, were calculated from the data in (b). Three independent replicates gave similar results and one typical data set is shown.

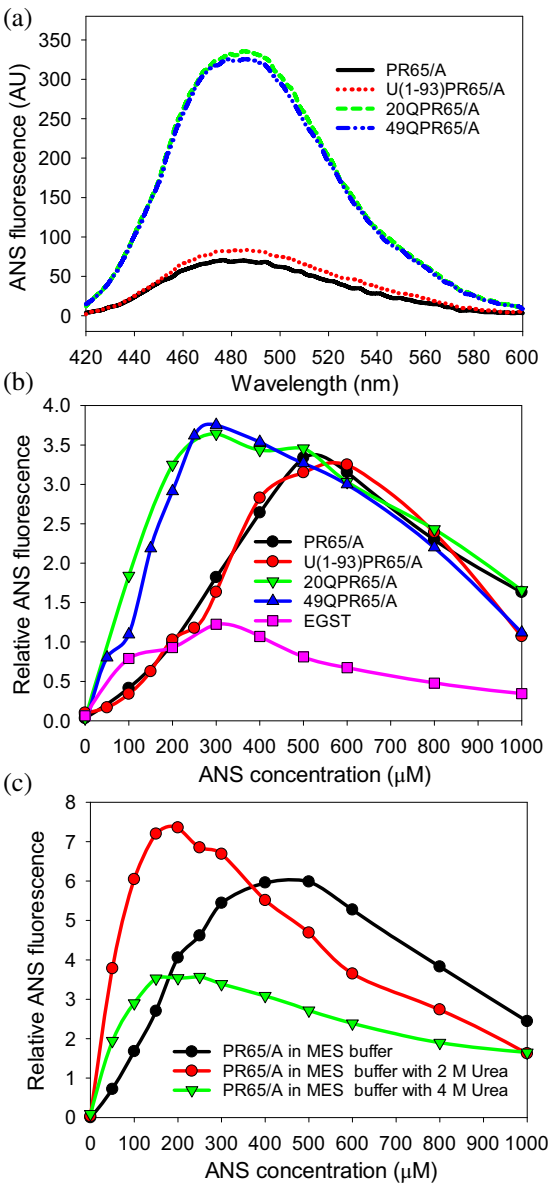

FIGURE 4 N-terminal fusion of HTT exon 1 increases the conformational flexibility of PR65/A upon binding of hydrophobic probe ANS. (a) ANS fluorescence emission spectra with excitation at 395 nm of 1 μM PR65/A, U(1-93)PR65/A, 20QPR65/A and 49QPR65/A in Buffer A (50 mM Tris–HCl buffer, pH 7.5, containing 150 mM NaCl and 2 mM DTT) containing 150 μM ANS. The curves were smoothed using the SigmaPlot software. (b) ANS binding to 0.4 μM PR65/A, U(1-93)PR65/A, 20QPR65/A, 49QPR65/A and EGST was monitored in Buffer A containing ANS of different concentrations by measuring the relative fluorescence intensity at 485 nm with excitation at 390 nm. (c) Binding of ANS to 0.4 μM native PR65/A, partially-denatured PR65/A with 2 M urea and partially-denatured PR65/A with 4 M urea were monitored in Buffer B (50 mM MES buffer, pH 6.5, containing 2 mM DTT) containing ANS of different concentrations, by measuring the fluorescence intensity at 485 nm with excitation at 390 nm. Three independent replicates gave similar results and one typical data set is shown.

smaller than for PR65/A and U1-93PR65/A (Figure 4b), indicating that the structures of 20QPR65/A and 49QPR65/A are more sensitive to the effects of ANS. The ANS binding properties of the four proteins are obviously different than the globular protein GST from *Escherichia coli* (EGST) which has a relative hydrophilic surface, indicating that the surface of the PR65/A structure has stronger hydrophobicity than EGST, and N-terminal fusion of HTT exon 1 enhances hydrophobicity on the surface of PR65/A structure (Figure 4b). ANS binding to native PR65/A and partially denatured PR65/A were compared. In 2 M urea, more hydrophobic surface of PR65/A was exposed showing stronger ANS binding fluorescence at lower concentration of ANS, whereas in 4 M urea, ANS binding fluorescence of PR65/A decreased with the further unfolding of PR65/A (Figure 4c), confirming that the disrupted PR65/A structure binds fewer molecules of ANS. Thus, N-terminal fusion of HTT exon 1 but not the Ure2 PrD may also increase the tendency of PR65/A to undergo structural changes upon ANS binding by decreasing the conformational stability of PR65/A.

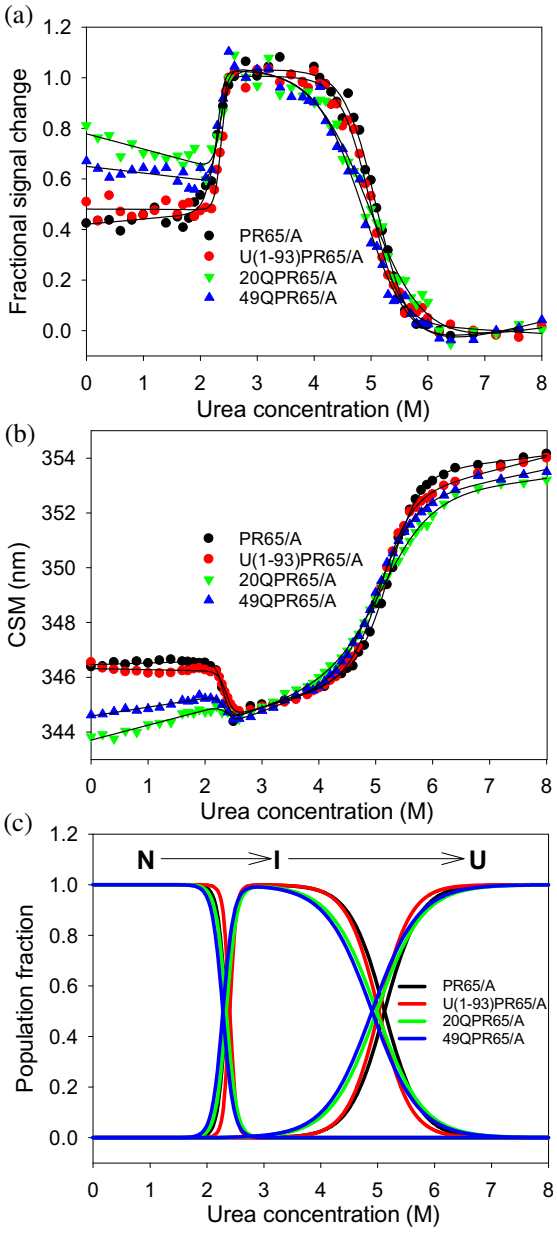

2.3 | N-terminal fusion of HTT exon 1 decreases the thermodynamic stability of PR65/A

Since the N-terminal fusion of HTT exon 1 perturbed the structure of PR65/A, the effect of N-terminal fusion of HTT exon 1 on thermodynamic stability of PR65/A was further studied. The reversible unfolding of PR65/A, U(1-93)PR65/A, 20QPR65/A and 49QPR65/A was examined, as previously described for PR65/A (Tsytlonok et al., 2013). The equilibrium unfolding transition of PR65/A, U(1-93)PR65/A, 20QPR65/A and 49QPR65/A was measured using urea as a denaturant and the intrinsic Trp fluorescence of the protein as a probe. We found that at pH 7.5 the unfolding of PR65/A was poorly reversible probably due to aggregation of an intermediate state, whereas at pH 6.5 the unfolding of PR65/A was basically reversible as described in the previous study (Tsytlonok et al., 2013). In 50 mM MES buffer (pH 6.5), two unfolding transitions were observed during the unfolding course of all of the four proteins with good reversibility, indicating population of an intermediate for each protein (Figure 5a–c).

FIGURE 5 N-terminal fusion of HTT exon 1 has some effect on the thermodynamic stability of PR65/A. Denaturation of 0.4 μM PR65/A, U(1-93)PR65/A, 20QPR65/A and 49QPR65/A with urea were monitored in Buffer B (50 mM MES buffer, pH 6.5, containing 2 mM DTT) containing urea of different concentrations at 25°C, by measuring the intrinsic fluorescence emission spectra between 300 and 400 nm with excitation at 280 nm. (a) Unfolding of PR65/A, U(1-93)PR65/A, 20QPR65/A and 49QPR65/A was monitored by measuring the intrinsic fluorescence intensity at 323 nm at different urea concentrations. Data were fitted to a three-state unfolding model via monomeric intermediate (N↔I↔U) as described in Section 4, and the resulting fit is shown as solid lines. The thermodynamic parameters obtained are shown in Table 2. (b) Unfolding of PR65/A, U(1-93)PR65/A, 20QPR65/A and 49QPR65/A were monitored by measuring the CSM of the intrinsic fluorescence spectra at different urea concentrations. Data were fitted to a three-state unfolding model via monomeric intermediate (N↔I↔U) as described in Section 4, and the resulting fit is shown as solid lines. (c) The fraction population of the native (N), intermediate (I) and unfolded (U) states during the unfolding course of PR65/A, U(1-93)PR65/A, 20QPR65/A and 49QPR65/A were calculated from the thermodynamic parameters shown in Table 2 (which were obtained from the fit shown in a). Three independent replicates gave similar results and one typical data set is shown.

To compare the unfolding and stability of PR65/A, U(1-93)PR65/A, 20QPR65/A and 49QPR65/A, we calculated the thermodynamic parameters from the unfolding curves at pH 6.5 from equilibrium denaturation. A three-state model was used to fit the data as described in Section 4—PR65/A has been shown previously to unfold via a hyper-fluorescent intermediate state (Tsytlonok et al., 2013). It is clear that the intermediate state of 20QPR65/A and 49QPR65/A is populated over a narrower range of urea concentrations compared to PR65/A and U(1-93)PR65/A (Figure 5a,b), suggesting that it is destabilized. The thermodynamic parameters obtained from the curve fitting of the four proteins were compared. The results show that they have similar m_1-values (m-values provide a measure of the increase in solvent-accessible surface area upon unfolding) and midpoint of the first transition and therefore similar $\Delta G_U(H_2O)_1$ (-Table 2). The m_2 value and midpoint of the second transition for 20QPR65/A or 49QPR65/A were slightly lower than for PR65/A and U(1-93)PR65/A, giving a lower $\Delta G_U(H_2O)_2$ and lower $\Delta G_U(H_2O)$ for 20QPR65/A or 49QPR65/A (Table 2). The fraction of intermediate was calculated using the m value and midpoint of the two transitions. As shown in Figure 5c, lower fractional population of the intermediate state of 20QPR65/A and 49QPR65/A was observed than for PR65/A and U(1-93) PR65A, which suggests that the N-terminal fusion of HTT exon 1 lowers the stability of the intermediate state of PR65/A. According to the published model for PR65/A unfolding, HEAT 1–2 and HEAT 11–13 are folded in the unfolding intermediate of PR65/A and unfold in the second transition (Tsytlonok et al., 2013). Our data therefore suggest that HTT exon 1 interacts with HEAT 1–2 or HEAT 11–13 of PR65/A and decreases the stability of these HEAT domains, and the length of Q stretch does not have a significant effect on this interaction.

2.4 | Interaction between HTT exon 1 and HEAT repeat structure during amyloid fibril formation

Next, the amyloid fibril formation of 49QPR65/A was measured *in vitro* to evaluate the effect of HEAT repeats on fibril formation of HTT exon 1. Different fibril formation conditions were tested, and the optimum conditions were in Buffer A (50 mM Tris–HCl buffer, pH 7.5, containing 150 mM NaCl and 2 mM DTT) at 37 or 30°C with shaking (with or without beads). We did not obtain fibrils when incubating under the same conditions in Buffer B (50 mM MES buffer, pH 6.5, containing 2 mM DTT).

The time course of fibril formation for 49QPR65/A was monitored by ThT fluorescence, ANS fluorescence,

TABLE 2 Parameters for the thermodynamic stability of PR65/A, U(1-93)PR65/A, 20QPR65/A and 49QPR65/A.

	[Protein] (μM)	m_1 (kcal mol^{-1} M^{-1})	$[Urea]_{1/2,1}$ (M)	m_2 (kcal mol^{-1} M^{-1})	$[Urea]_{1/2,2}$ (M)	$\Delta G_U(H_2O)_1$ (kcal mol^{-1})	$\Delta G_U(H_2O)_2$ (kcal mol^{-1})	$\Delta G_U(H_2O)$ (kcal mol^{-1})
PR65/A	0.4	7.7 ± 0.7[a]	2.34 ± 0.03[a]	1.93 ± 0.09[a]	5.12 ± 0.05[a]	18.2 ± 2.0[a]	9.9 ± 0.4[a]	28.1 ± 2.0[a]
		6.8 ± 0.7[b]	2.32 ± 0.02[b]	2.02 ± 0.04[b]	5.27 ± 0.05[b]	15.7 ± 1.6[b]	10.6 ± 0.2[b]	26.4 ± 1.5[b]
U(1-93) PR65/A	0.4	10.5 ± 0.6[a]	2.40 ± 0.02[a]	2.11 ± 0.11[a]	5.02 ± 0.03[a]	25.1 ± 1.4[a]	10.6 ± 0.5[a]	35.7 ± 1.2[a]
		8.8 ± 0.1[b]	2.40 ± 0.02[b]	2.09 ± 0.04[b]	5.15 ± 0.03[b]	21.2 ± 0.4[b]	10.8 ± 0.2[b]	32.0 ± 0.3[b]
20QPR65/A	0.4	6.5 ± 1.3[a]	2.34 ± 0.03[a]	1.46 ± 0.07[a]	4.98 ± 0.02[a]	15.3 ± 3.2[a]	7.3 ± 0.4[a]	22.6 ± 3.2[a]
		6.5[b,c]	2.32 ± 0.01[b]	1.22 ± 0.04[b]	5.22 ± 0.01[b]	15.1 ± 0.1[b]	6.4 ± 0.2[b]	21.4 ± 0.2[b]
49QPR65/A	0.4	6.3 ± 0.3[a]	2.28 ± 0.02[a]	1.45 ± 0.16[a]	4.90 ± 0.01[a]	14.4 ± 0.7[a]	7.1 ± 0.8[a]	21.5 ± 1.2[a]
		6.3[b,c]	2.31 ± 0.01[b]	1.27 ± 0.05[b]	5.09 ± 0.04[b]	14.6 ± 0.1[b]	6.5 ± 0.3[b]	21.1 ± 0.3[b]

Note: Folding was monitored by intrinsic fluorescence. Data were fitted to a three-state unfolding model via monomer intermediate (N↔I↔U). The data shown are the mean of fit results from at least three independent experiments and the error represents the standard error of the mean. m is the slope of the transition and $[Urea]_{1/2}$ is the midpoint; $\Delta G_U(H_2O)_1 = m_1 \times [Urea]_{1/2,1}$; $\Delta G_U(H_2O)_2 = m_2 \times [Urea]_{1/2,2}$; $\Delta G_U(H_2O) = \Delta G_U(H_2O)_1 + \Delta G_U(H_2O)_2$ for a three-state model. Free energy values for unfolding are shown for standard conditions, that is, 1 M protein concentration.

[a]Folding and unfolding of the proteins was monitored by measuring the intrinsic fluorescence intensity at 323 nm with excitation at 280 nm.

[b]Folding and unfolding of the proteins was monitored by measuring the CSM of intrinsic fluorescence spectra with excitation at 280 nm.

[c]CSM data were fitted to a three-state model by using m_1 of fixed value (which was the mean of fitted m_1 from the intrinsic fluorescence intensity data) for 20QPR65/A and 49QPR65/A, as fitting of a very short first transition cannot give a reliable m_1 value.

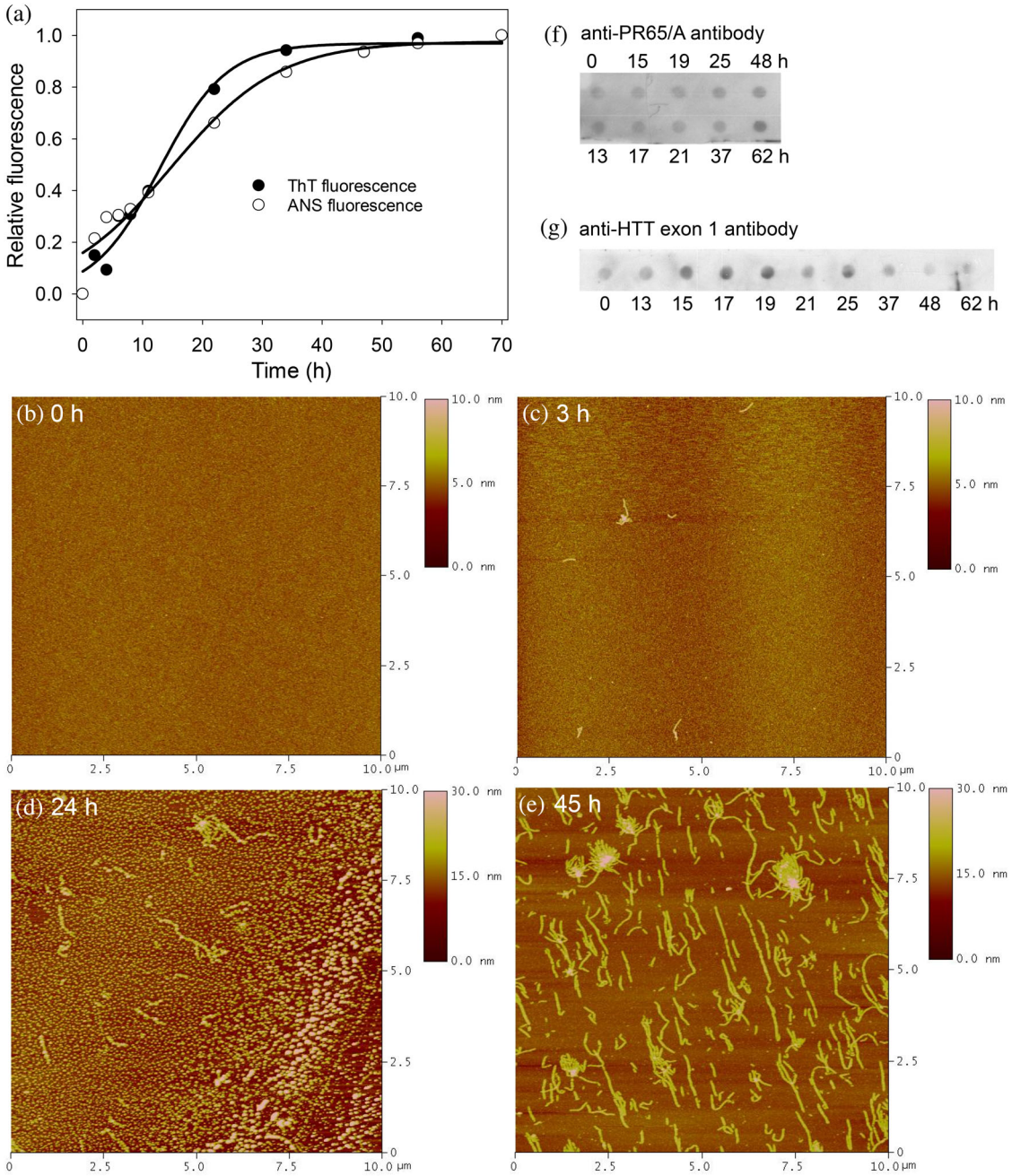

FIGURE 6 Amyloid fibril formation of 49QPR65/A. Fibril formation of 18 μM 49QPR65/A was performed at 37°C in Buffer A (50 mM Tris–HCl buffer, pH 7.5, containing 150 mM NaCl and 2 mM DTT) with shaking. (a) The time course of 49QPR65/A fibril formation was monitored by ThT fluorescence and ANS fluorescence. (b–e) AFM detection of 49QPR65/A fibril formation. 10 μm × 10 μm square scan areas were randomly taken from the 0 h (b), 3 h (c), 24 h (d), and 45 h (e) samples for analysis by AFM. (f, g) The time course of 49QPR65/A fibril formation detected by filter retardation assay with anti-PR65/A antibody (f) and anti-HTT exon 1 antibody (g). Three independent replicates gave similar results and one typical data set is shown.

AFM and filter retardation assay. The time course of 49QPR65/A fibril formation showed a typical sigmoidal curve, with a very short lag phase, very long logarithmic phase and then a plateau phase (Figure 6a). This is consistent with the hypothesis that during fibril formation of HTT exon 1, the initial formation of oligomers exhibits non-nucleated, downhill kinetics (Thakur et al., 2009; Chen and Wolynes, 2017). The ANS-fluorescence showed a similar profile to the ThT-fluorescence curve (Figure 6a), indicating that the increase in hydrophobic surface is concomitant with β-sheet structure formation during the fibril formation of 49QPR65/A. AFM detection showed that there were no soluble aggregates at the beginning of the 49QPR65/A fibril formation (Figure 6b).

After 3 h of incubation, some short fibrils appeared (Figure 6c), in accordance with the ThT result. At the mid-time of the logarithmic phase, a large number of spherical aggregates formed (Figure 6d), followed by formation of numerous long fibrils (Figure 6e). The height of fibrils increased during the course of fibril formation and the final fibril height was 11–17 nm, measured from the AFM images. In the filter retardation assay, SDS-resistant aggregates were detected using anti-HTT exon 1 antibody and anti-PR65/A antibody (Figure 6f,g), which confirmed that the two parts of the chimeric protein are present in the fibrils. It was observed that the color development of detection with anti-PR65/A antibody was basically consistent with the time course of 49QPR65/A fibril formation, but for the detection with anti-HTT exon 1 antibody the strongest signal appeared at the time points of 15, 17, and 19 h (in the middle of the logarithmic phase), and after these time points the signal decreased with time (Figure 6f,g). This suggests that the fibril core formed by HTT exon 1 is buried within the structure of mature fibrils and PR65/A is wrapped around the fibril core.

In view of the above results showing that HTT exon 1 can interact with the HEAT repeat structure of PR65/A, we then investigated the effect of HEAT repeats on fibril formation of HTT exon 1 and also the effect of fibril formation of HTT exon 1 on the structure of PR65/A. We found fibril formation of 49QPR65/A was much slower than for the isolated 49 Q HTT exon 1 (induced by cleavage of the GST tag from GST-49 Q HTT exon 1), and 49QPR65/A formed longer fibrils than 49 Q HTT exon 1 (Figure 7a,c). We also noticed that 49 Q HTT exon 1 fibrils can form bundles as well as having multiple ends, and the height of fibrils is below 10 nm as shown by the AFM images (Figure 7c,d), which is similar to the previously reported HTT exon 1 fibrils (Wagner et al., 2018; Silva et al., 1986), although the 49 Q HTT exon 1 fibrils are shorter and have fewer bundles than the previously reported HTT exon 1 fibrils. However, 49QPR65/A fibrils only rarely form bundles or show branching (Figure 7a). This indicates that the fused PR65/A which is arranged outside of the fibril core changes the higher-order architecture of the fibrils and the kinetics of fibril formation. The average length and the degree of branching may be determined by the dominant pathway of amyloid nucleation. Usually, a higher primary nucleation rate causes the formation of a larger amounts of amyloid nuclei at the initial stage of aggregation and so the average length of the fibrils will be shorter, while a slower primary nucleation rate leads to less elongation-competent nuclei and so the average fibril length will be longer. Moreover, the presence of surface-catalyzed secondary nucleation can lead to branching of the fibrils, while the fibril core of the

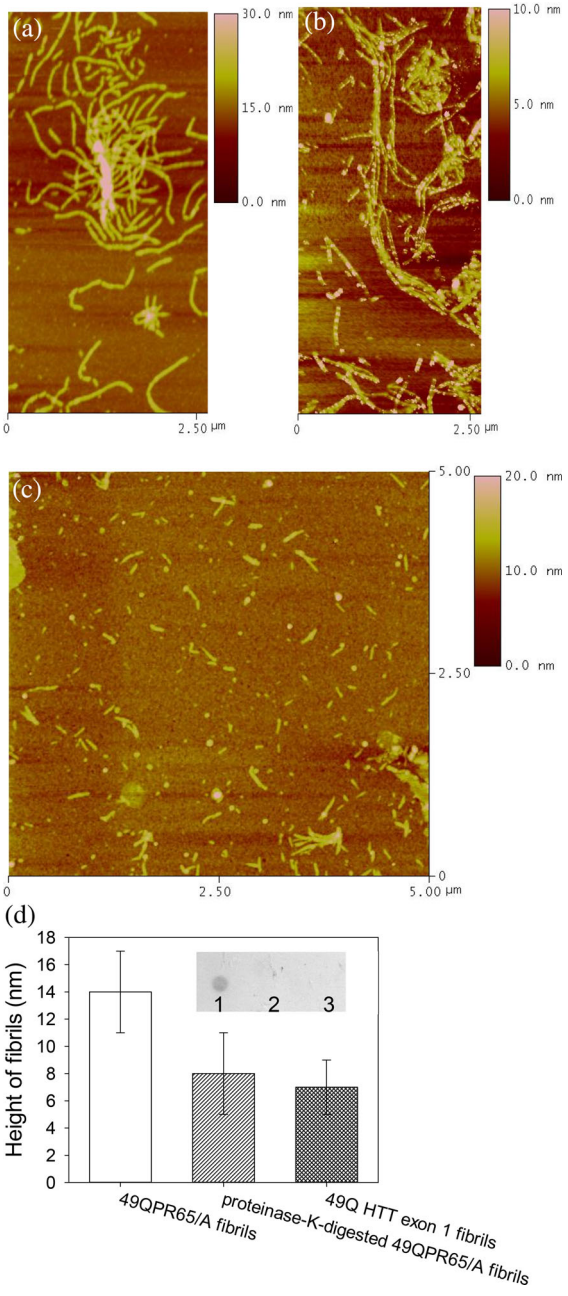

FIGURE 7 Comparison of 49QPR65/A fibrils and 49 Q HTT exon 1 fibrils. (a, b) Fibril formation of 49QPR65/A was performed as in Figure 6, and 5 μm × 2.5 μm scan areas were randomly taken from 48 h samples for AFM analysis before (a) and after (b) proteinase K digestion for 24 h at 37°C. (c) Fibril formation of 18 μM 49Q HTT exon 1 was performed at 37°C in Buffer A (50 mM Tris–HCl buffer, pH 7.5, containing 150 mM NaCl and 2 mM DTT) without shaking. Fibril formation was initiated by cleavage of the GST tag with thrombin, and 5 μm × 5 μm square scan areas were randomly taken from the 24 h samples. (d) The fibril height of 49QPR65/A fibrils, proteinase-K-digested 49QPR65/A fibrils and 49Q HTT exon 1 fibrils, obtained from AFM scan area of panels (a–c), shown as average and standard deviations ($n = 10$–20). Filter retardation assay with anti-PR65/A antibody of 49QPR65/A fibrils, proteinase-K-digested 49QPR65/A fibrils and 49Q HTT exon 1 fibrils are shown as 1, 2 and 3 of the inset panel. Three independent replicates gave similar results and one typical data set is shown.

49QPR65/A is probably wrapped around by the fused PR65/A domain, which could prevent surface-catalyzed secondary nucleation and branching of the fibrils.

49QPR65/A fibrils were digested with proteinase K to explore the possible composition of the fibril core since the fibril core is protease-resistant. The fibril height of proteinase-K-digested 49QPR65/A fibrils was similar to 49 Q HTT exon 1 fibrils, and lower than 49QPR65/A fibrils, and the proteinase-K-digested 49QPR65/A fibrils were not reactive to anti-PR65/A antibody similar to 49 Q HTT exon 1 fibrils (Figure 7a–d). The fibril formation of 49QPR65/A can be greatly accelerated by seeding with 49QPR65/A fibril seeds or 49 Q HTT exon 1 fibril seeds, whereas 20QPR65/A cannot form amyloid fibrils even in the presence of 49QPR65/A fibril seeds or 49 Q HTT exon 1 fibril seeds, as detected by ThT fluorescence and filter retardation assay with anti-PR65/A antibody (Figure 8a,b). If wrapping of PR65/A around the fibril core prevents surface-catalyzed secondary nucleation and results in dominant seed-templated elongation, then the cross-seeding results indicate that fibrils of 49QPR65/A and 49 Q HTT exon 1 may possess similar fibril cores. However, we still lack direct structural data to confirm this. Therefore, we conclude that the fusion of C-terminal PR65/A did not alter the fibril-formation ability of HTT exon 1, but changed the kinetics of fibril formation and the higher-order architecture of the fibrils.

To check whether the structure of PR65/A changed during the fibril formation of 49QPR65/A, we used ANS fluorescence as a probe. The ANS binding curve for 49QPR65/A fibrils and native 49QPR65/A were compared, showing that 49QPR65/A fibrils are more sensitive to ANS at very low concentration than native 49QPR65/A (Figure 9a), although the two states of 49QPR65/A had similar saturation points for ANS binding (Figure 9b). The intensity of ANS fluorescence of proteinase-K-digested 49QPR65/A fibrils was quite low compared with native 49QPR65/A or 49QPR65/A fibrils (Figure 9a) while ANS fluorescence of 49QPR65/A increased significantly during the fibril formation (Figures 6a and 9a). When the ANS binding spectra of native 49QPR65/A and proteinase-K-digested 49QPR65/A fibrils were added together, the combined fluorescence intensity was still lower than the ANS fluorescence intensity of 49QPR65/A fibrils (Figure 9a), suggesting that the structure of PR65/A changes during fibril formation resulting in enhanced ANS binding.

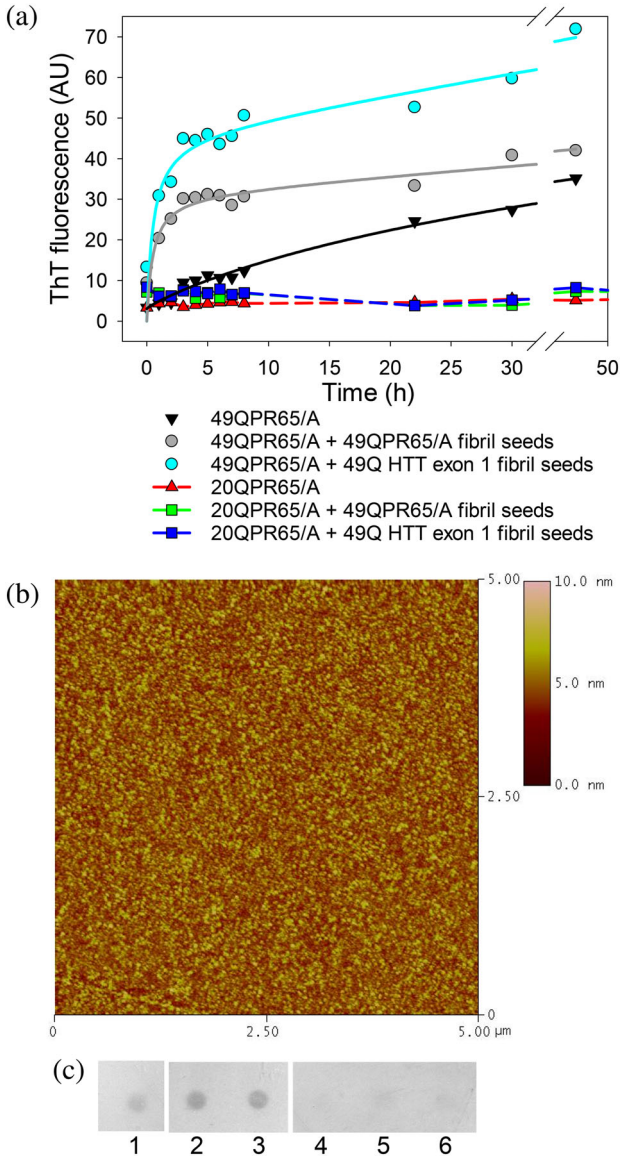

FIGURE 8 Comparison of fibril formation of 49QPR65/A and 20QPR65/A. (a) Fibril formation of 16 µM 49QPR65/A and 20QPR65/A in the absence or presence of 1.6 µM 49QPR65/A fibril seeds or 49Q HTT exon 1 fibril seeds was monitored by ThT binding assay. Fibril formation was performed as in Figure 6. (b) AFM analysis of 20QPR65/A after 42-h shaking at 37°C in Buffer A (50 mM Tris–HCl buffer, pH 7.5, containing 150 mM NaCl and 2 mM DTT) is shown in 5 µm × 5 µm square scan areas. (c) Filter retardation assay with anti-PR65/A antibody is shown as: (1) 49QPR65/A fibrils without seeding; (2) 49QPR65/A fibrils seeded by 49QPR65/A fibril seeds; (3) 49QPR65/A fibrils seeded by 49Q HTT exon 1 fibril seeds; (4) 20QPR65/A after fibril formation without seeding; (5) 20QPR65/A after fibril formation seeded by 49QPR65/A fibril seeds; (6) 20QPR65/A after fibril formation seeded by 49Q HTT exon 1 fibril seeds. Three independent replicates gave similar results and one typical data set is shown.

3 | DISCUSSION

The effect of HTT exon 1 and an extended poly Q tract on the structure and function of HTT is hard to study directly due to the large size of the HTT protein, together with its conformational heterogeneity and tendency to aggregate (Guo et al., 2018; Harding et al., 2019; Li

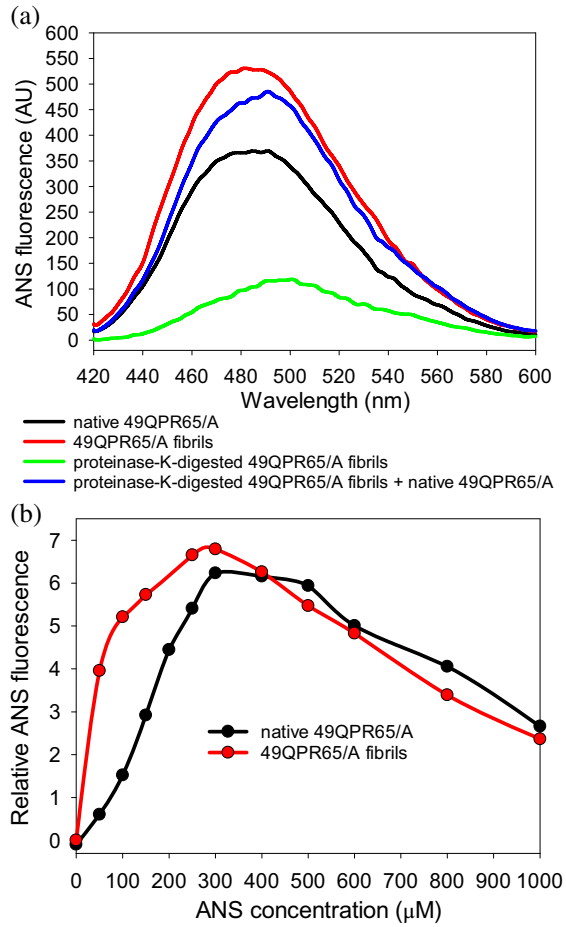

FIGURE 9 Fibril formation of 49QPR65/A increases its conformation flexibility upon binding of the hydrophobic probe ANS. (a) ANS fluorescence emission spectra with excitation at 395 nm of 1 μM native 49QPR65/A, 49QPR65/A fibrils and proteinase-K-digested 49QPR65/A fibrils were measured in Buffer A (50 mM Tris–HCl buffer, pH 7.5, containing 150 mM NaCl and 2 mM DTT) containing 150 μM ANS. Individual ANS fluorescence spectra of native 49QPR65/A and proteinase-K-digested 49QPR65/A fibrils were added to generate the predicted spectrum of the mixture. The curves were smoothed using the SigmaPlot software. (b) ANS binding to 1 μM native 49QPR65/A and 49QPR65/A fibrils was monitored in Buffer A containing ANS of different concentrations by measuring fluorescence intensity at 485 nm with excitation at 390 nm. Three independent replicates gave similar results and one typical data set is shown.

et al., 2006). Using a fusion between cellular retinoic acid binding protein I (CRABP I) and HTT exon 1, researchers found that extended polyQ tracts cause aggregation of CRABP I and perturbation of the adjacent β-barrel structure (Ignatova and Gierasch, 2006). In this study we constructed chimeras of HEAT repeat protein PR65/A with N-terminal fusion of 20 Q or 49 Q HTT exon 1 as model proteins to mimic wild-type or mutant HTT in the context of adjacent HEAT repeat structure as is found in HTT. It is surprising to find that 20 Q or 49 Q HTT exon 1 both disturbed the structure of PR65/A to a similar extent. Consistent with this study, the length of Q stretch also did not affect the EM structure of the complex of HTT and HAP40 or the thermal stability of HTT (Guo et al., 2018; Harding et al., 2019), and monomeric HTT exon 1 has similar overall structural features for wild-type and pathological lengths of Q stretch (Warner et al., 2017). However another study found that 78 Q HTT has a different global structure than 23 Q HTT, suggesting the polyQ expansion induces global structural changes within the HTT domains (Jung et al., 2020). Therefore, the effect of polyQ expansion on the interaction between HTT exon 1 and the following heat repeat structure is worthy of further study.

The interaction between HTT exon 1 and HEAT repeat structure of PR65/A was verified by the slight structural perturbance of PR65/A caused by N-terminal fusion of HTT exon 1, and measured by SEC, intrinsic fluorescence, CD and thermostability. Similar to HTT exon 1, the Ure2 PrD is also an intrinsically disordered region, but it did not affect the structure of PR65/A, indicating some specificity of the interaction between HTT exon 1 and HEAT repeat structure. The interaction between HTT exon 1 and HEAT repeat structure of PR65/A led to some destabilization and expansion of the HEAT repeat structure, thus decreasing the conformational stability of PR65/A and increasing sensitivity to environmental changes including salt concentration and hydrophobic interactors. Conformational flexibility of PR65/A is the basis for PR65/A to accommodate its different partners, as indicated by available structures of PR65/A in different assemblies (Cho and Xu, 2007; Chen et al., 2007; Xu et al., 2008). Conformational flexibility of PR65/A also helps regulate functions of its interacting proteins, such as enzyme activity, which is exemplified by the fact that PR65/A can act as elastic connector linking force and catalysis (Kaynak et al., 2023; Grinthal et al., 2010). Similar to PR65/A, HTT is a complex scaffold protein with multiple interaction partners and can also participate in modulating activity of its clients (Wanker et al., 2019; Proskura et al., 2017). Understanding the mechanisms of subtle modulations of HTT on protein–protein interactions and related cellular networks, as well as their alteration in HD, is essential for explaining the labyrinthine pathology of HD (Wanker et al., 2019; Proskura et al., 2017). The results from this study will provide valuable information for further study. It can be speculated that interaction of HTT exon 1 with the cellular membrane, fibril formation of HTT exon 1 as well as PTMs within HTT exon 1 or the adjacent HEAT repeat structure could modulate function of HTT by

modulating the interaction between HTT exon 1 and the HEAT repeat structure.

HTT fragment length is also a critical factor for aggregation in HD, besides the number of Q and expression level of the *HTT* gene, as indicated by in vivo studies (Hackam et al., 1998; Li and Li, 1998; Li et al., 2001; Chen et al., 2017). HTT exon 1 attached to GST or a β-barrel protein can still form fibrils, as detected in *in vitro* studies, which indicates that HTT exon 1 with an appended folded domain can still form fibrils (Scherzinger et al., 1997; Ignatova and Gierasch, 2006). In this study 49QPR65/A formed typical amyloid fibrils under certain conditions but not 20QPR65/A, which is consistent with the fact that aggregation and HD onset occurs *in vivo* when the number of Q residues is over 35. Although the tendency of HTT exon 1 to form fibrils is not affected by covalent attachment of HEAT repeats, attachment of PR65/A substantially changed the aggregation kinetics of HTT exon 1 and the morphology of fibrils. Analysis of inclusions in HD reveals that the N-terminus of HTT is the major component of nuclear aggregates, and both full-length HTT and fragments of HTT exist in cytoplasmic aggregates (Hackam et al., 1998; Cooper et al., 1998; Martindale et al., 1998). This study suggests that it is possible for full-length mutant HTT or truncated HTT containing HTT exon 1 and the downstream HEAT repeat structure to initialize amyloid fibril formation in HD pathology. It has been reported that *in vivo* the presence of short N-terminal HTT fragments increases the frequency of aggregation (Hackam et al., 1998). In this study fibril formation of 49QPR65/A could be seeded not only by fibril seeds formed from itself but also by fibril seeds formed from 49 Q HTT exon 1, which suggests that fibril formation of long HTT fragments can be accelerated by fibril formation of short N-terminal HTT fragments. Abnormal proteolysis of mutant HTT is often detected in HD (Dyer and McMurray, 2001; Kim et al., 2001; Kim et al., 2006; Wellington et al., 2002). Decreased proteolysis leads to a reduction in elimination of aggregates (Dyer and McMurray, 2001), but increased proteolysis accelerates fragmentation of HTT and facilitates aggregation of short N-terminal HTT fragments (Kim et al., 2001, 2006; Wellington et al., 2002). Abnormal proteolysis of mutant HTT could accelerate the HD disease process by producing accumulation of exon 1 fragment to seed the aggregation (Landles et al., 2010).

PR65/A chimera with N-terminal fusion of HTT exon 1 provide a new model for HD research. This study applying chimeric models suggests that interaction between HTT exon 1 and HEAT repeat structure may be involved in the normal function of HTT as well as influencing the pathological process of HD. This model can be further employed in related research, such as determination of fibril structure, and study of the fibril formation mechanism and its relationship to fibril cytotoxicity.

4 | EXPERIMENTAL PROCEDURES

4.1 | Protein expression and purification

HTT exon 1 genes containing 20 Q and 51 Q (coding MATLEKLMKAFESLKSF**[Qn]**P14QLPQPPPQAQPLLPQ PQPPPPPPPPPPGPAVAEEPLHRP) were gifts from Erich Wanker (Max Delbrueck Center for Molecular Medicine, Berlin, Germany), and the *PR65/A* gene was a gift from David Barford (ICR, London, UK). HTT exon 1 genes containing 20 Q and 51 Q were inserted into the pGEX-4T-1 plasmid using the BamHI and NotI sites (forward primer: 5′ gctcgc **ggatcc** atggcgaccctggaaaagctg 3′, reverse primer: 5′ acgatt **gcggccgc** tcatta ctcgag tggtcggtgcagcggctcc 3′) to generate *GST*-20Q *HTT* exon 1 and *GST*-49Q *HTT* exon 1 DNA respectively. (After the HTT exon 1 gene containing 51 Q was inserted, 2 Q were missing and so it became HTT exon 1 containing 49 Q.) In the expressed fusion proteins, the linker between GST and HTT exon 1 is "SDLVPRGS" (where "LVPRGS" is the thrombin cleavage site) and there are two extra amino acid residues "LE" at the C terminal of HTT exon 1. The *PR65/A* gene was inserted into pGEX-4T-1-*GST*-20Q *HTT* exon 1 and pGEX-4T-1-*GST*-49Q *HTT* exon 1 plasmids using the XhoI and NotI sites (forward primer: 5′ aactgg **ctcgag** atggcggcggccgacggcgacg 3′, reverse primer: 5′ acgatt **gcggccgc** ttatcaggcgagagacagaacag 3′) to generate GST-20Q*PR65/A* and GST-49Q*PR65/A* chimeric DNA constructs, respectively. The linker between *HTT* exon 1 and *PR65/A* is the XhoI site (ggatcc) and the translated amino acid residues are "LE". The DNA for *GST*-20Q *HTT* exon 1 and *GST*-49Q *HTT* exon 1, as well as *GST*-20Q*PR65/A* and *GST*-49Q*PR65/A* was inserted into the mini-pRSETa plasmid (a gift from Dr Mark Bycroft, Centre for Protein Engineering, Cambridge, UK) using the EcoRI and HindIII sites for expression of His6-GST-20Q HTT exon 1, His6-GST-49Q HTT exon 1, His6-GST-20QPR65/A and His6-GST-49QPR65/A, respectively. *PR65/A*, 20Q*PR65/A* and 49Q*PR65/A* DNA was inserted into the mini-pRSETa plasmid using the BamHI and HindIII sites to express His6-PR65/A, His6-20QPR65/A and His6-49QPR65/A respectively (Figure 1b). The U(1-93)*PR65/A* chimeric DNA construct was generated by inserting the gene of the N-terminal 93 aa of Ure2 (Perrett and Jones, 2008) into the pRSETa-20Q*PR65/A* plasmid to replace 20Q *HTT* exon 1 using the BamHI and XhoI sites to express His6-U(1-93)PR65/A (Figure 1b). The linker between *Ure2* PrD and *PR65/A* is also the XhoI site (ggatcc) which is translated to "LE" in

the expressed protein. The His6 tag in the fusion proteins is uncleavable and the extra sequence before PR65/A, HTT exon 1 or Ure2 PrD is "MRGSHHHHHHGLV PRGS". The extra sequence before GST is "MRGSHHHH HHGLVPRGSELDICSWYL" which is removed together with GST after thrombin cleavage.

E. coli strain BL21(DE3) Codon Plus cells transformed with the above expression plasmids were grown at 37°C and induced with 0.1 mM 1-thio-β-D-galactopyranoside (IPTG) when the OD_{600} reached 0.5–0.8. The cells were grown for a further 12 h before harvesting and then lysed using a JNBIO JN-3000 PLUS high-pressure cell press.

PR65/A and PR65/A chimeric proteins were purified as described for purification of PR65/A (Groves et al., 1999). Briefly, the proteins were purified with a Ni-NTA column step, an anion exchange step and a final SEC step. The cleared cell lysate in Buffer C (50 mM Tris–HCl buffer, pH 7.5, containing 300 mM NaCl, 20 mM imidazole and 2 mM β-mercaptoethanol) was applied to a Ni-NTA column (chelating Sepharose fast-flow resin, GE Healthcare Science), and the protein was eluted using a linear gradient to 300 mM imidazole. The eluate was diluted 10-fold with Buffer D (50 mM Tris–HCl buffer, pH 7.5, containing 2 mM DTT and 2 mM EDTA) and was applied to a SOURCE 15Q anion exchange column (GE Healthcare Science), and the protein was eluted using a linear gradient to 1 M NaCl. Peak fractions containing PR65/A or PR65/A chimeric proteins were pooled, concentrated to a volume of ~1 mL and loaded onto a Superdex 200 HiLoad column (GE Healthcare Science) equilibrated with Buffer A (50 mM Tris–HCl buffer, pH 7.5, containing 150 mM NaCl and 2 mM DTT). The presence of PR65/A or PR65/A chimeric proteins was confirmed by 10% SDS-PAGE after each purification step. His6-GST-20Q HTT exon 1, His6-GST-49Q HTT exon 1 and His6-GST-49QPR65/A were purified using an Ni-NTA column as described in the above Ni-NTA column step for purification of PR65/A and PR65/A chimeric proteins. Then the eluate was dialyzed into Buffer A. GST-20Q HTT exon 1, GST-49Q HTT exon 1 and GST-49QPR65/A were purified using a Glutathione (GSH) Agarose column (GE Healthcare Science). The cleared cell lysate in buffer E (50 mM Tris–HCl buffer, pH 7.5, containing 150 mM NaCl and 2 mM β-mercaptoethanol) was applied to a Glutathione Agarose column. The column was washed with Buffer E and eluted with Buffer F (50 mM Tris–HCl buffer, pH 7.5, containing 150 mM NaCl, 15 mM GSH and 2 mM β-mercaptoethanol). The eluate was also dialyzed into Buffer A.

All protein concentrations (in terms of monomers) were measured by absorbance at 280 nm using calculated extinction coefficients (Gill and von Hippel, 1989). PR65/A, U(1-93)PR65/A, 20QPR65/A and 49QPR65/A have the same calculated extinction coefficient of 43,275 $M^{-1}\,cm^{-1}$. The calculated extinction coefficient for GST-20Q HTT exon 1 and GST-49Q HTT exon 1 is 43,110 $M^{-1}\,cm^{-1}$, and GST-49QPR65/A has a calculated extinction coefficient of 86,385 $M^{-1}\,cm^{-1}$. *E. coli* GST (EGST) was expressed and purified as described (Wang et al., 2009). All proteins were stored at −80°C in Buffer A and defrosted in a 25°C water bath immediately prior to use.

4.2 | Analytical size exclusion chromatography

Purified proteins of 10 μM (100 μL) were loaded onto a 24-mL Superdex 200 HiLoad column (GE Healthcare Science) equilibrated with Buffer A or Buffer B (50 mM MES buffer, pH 6.5, containing 2 mM DTT) to determine their oligomeric state. Blue dextran (2000 kDa), β-amylase (200 kDa), alcohol dehydrogenase (150 kDa), BSA (66 kDa), carbonic anhydrase (29 kDa) and cytochrome C (12.4 kDa) were used as molecular mass standards.

4.3 | Sedimentation equilibrium

Sedimentation analysis was performed in 50 mM Tris–HCl buffer, pH 7.5, containing 150 mM NaCl and 1 mM DTT or 50 mM MES buffer, pH 6.5, containing 1 mM DTT with protein concentrations of 5 and 10 μM, scanning at 280 nm, using a Beckman XL-1 analytical ultracentrifuge with an An-60Ti analytical rotor. Sedimentation equilibrium experiments were performed at 10,000 rpm, with overspeeding at 15,000 rpm for 4 h to speed up the attainment of equilibrium. Scans were taken at intervals of 4 h (during the day) or 16 h (overnight), until successive scans superimposed exactly, when the later scan was taken as being operationally at equilibrium. The molecular weight of proteins was calculated based on nonlinear least squares fitting using the software provided with the instrument.

4.4 | Intrinsic fluorescence measurements

Intrinsic fluorescence spectra of the proteins were obtained between 300 and 400 nm with excitation at 280 nm, measured using a Shimadzu RF-5301PC spectrofluorometer. Spectra of 0.4 μM proteins were measured in 50 mM Tris–HCl buffer (pH 7.5) or 50 mM MES buffer

(pH 6.5) containing different concentrations of NaCl and 2 mM DTT at 25°C in a thermostatted cuvette.

In the unfolding experiments, spectra of 0.4 μM proteins in 50 mM MES buffer, pH 6.5, containing a series of concentrations of urea and 2 mM DTT were scanned, after the samples were allowed to pre-equilibrate at 25°C for 3 h. For the renaturation experiment, the proteins were pre-denatured in 8 M urea. The concentration of urea solutions was confirmed using an Abbe refractometer. The maximum change in the intensity of intrinsic fluorescence during the denaturation was observed at 323 nm, which was therefore used to monitor the change in fluorescence intensity over the course of denaturation. Data were also represented as the CSM, which is sensitive to changes in the maximum emission wavelength, and has an improved signal to noise ratio (Silva et al., 1986). The CSM of intrinsic fluorescence was calculated using the following formula:

$$\mathrm{CSM} = \frac{\sum_{i=300}^{400} i \times \mathrm{IF}_i}{\sum_{i=300}^{400} \mathrm{IF}_i}$$

4.5 | Data analysis of the equilibrium unfolding transition

The data of the intrinsic fluorescence measurements were fitted to a three-state unfolding model via monomeric intermediate (N↔I↔U) according to the two transitions observed and the monomer state of native PR65/A, U(1-93)PR65/A, 20QPR65/A and 49QPR65/A. The three-state unfolding model via monomeric intermediate is described below. In each case, nonlinear least-squares fitting of the data was carried out using the regression wizard of the SigmaPlot software.

The amplitude of the spectroscopic signal or CSM value determined at each denaturant concentration was assumed to be a linear combination of the fractional contribution from each species:

$$y = f_N(y_N + m_N[\mathrm{Urea}]) + f_I(y_I + m_I[\mathrm{Urea}]) + f_U(y_U + m_U[\mathrm{Urea}]) \quad (1)$$

where y_N, y_I, y_U, m_N, m_I, and m_U are the intercepts and slopes of the initial baseline, intermediate state and final baselines, respectively; and f_N, f_I, and f_U are the fraction of native, intermediate and denatured states, respectively. The derivation of the expression for f_N, f_I, and f_U is outlined below.

The equilibrium constants for the two transitions are given by $K_1 = [I]/[N] = f_I/f_N$ and $K_2 = [U]/[I] = f_U/f_I$. The total protein concentration is $C = [N] + [I] + [U]$ and $f_N + f_I + f_U = 1$. Hence $f_N = [N]/C$, $f_I = [I]/C$ and $f_U = [U]/C$. From this it can be seen that: $f_N = f_I$, K_1 and $f_U = f_I$, K_2. Then the fraction population can be given:

$$f_N = \frac{1}{1 + K_1 + K_1K_2} \quad (2)$$

$$f_I = \frac{K_1}{1 + K_1 + K_1K_2} \quad (3)$$

$$f_U = \frac{K_1K_2}{1 + K_1 + K_1K_2} \quad (4)$$

The free energy for unfolding, $\Delta G_U = -RT\ln K$, shows a linear relationship with the denaturant concentration:

$$\Delta G_U = \Delta G_U(H_2O) - m[\mathrm{Urea}] \quad (5)$$

where m is the denaturant dependence (or slope) of the transition and $\Delta G_U(H_2O)$ is the free energy of unfolding in the absence of denaturant. The denaturant mid-point of the curve, $[\mathrm{Urea}]_{1/2}$, is a useful parameter as it has a lower inherent error than $\Delta G_U(H_2O)$ and so can allow detection of small differences in stability between conservative mutants of the same protein when measured under the same solution conditions. Assuming the two transitions are distinct, the mid-point of the first transition occurs when $f_N = f_I = 1/2$ and so $K_1 = 1$, hence:

$$\Delta G_U(H_2O)_1 = m_1[\mathrm{Urea}]_{1/2,1} \quad (6)$$

$$K_1 = \exp\left[\frac{m_1}{RT}\left([\mathrm{Urea}] - [\mathrm{Urea}]_{1/2,1}\right)\right] \quad (7)$$

Similarly, the mid-point of the second transition occurs when $f_I = f_U = 1/2$ and so $K_2 = 1$, hence:

$$\Delta G_U(H_2O)_2 = m_2[\mathrm{Urea}]_{1/2,2} \quad (8)$$

$$K_2 = \exp\left[\frac{m_2}{RT}\left([\mathrm{Urea}] - [\mathrm{Urea}]_{1/2,2}\right)\right] \quad (9)$$

Fitting of the data to Equation (1) was carried out to obtain ten unknown parameters, after substituting for f_N, f_I, and f_U in terms of m_1, m_2, $[\mathrm{Urea}]_{1/2,1}$ and $[\mathrm{Urea}]_{1/2,2}$, using the expression given in Equations (2)–(4), (7) and (9), where m_1 and m_2 are the slopes, and $[\mathrm{Urea}]_{1/2,1}$ and $[\mathrm{Urea}]_{1/2,2}$ are the mid-points of the first and second transitions, respectively. The overall stability of the protein according to this model is obtained from: $\Delta G_U(H_2O) = \Delta G_U(H_2O)_1 + \Delta G_U(H_2O)_2$.

4.6 | CD measurements

Far-UV CD spectra were measured at 25°C in a 0.1 cm path-length thermostatted cuvette using a Pistar-180 instrument (Applied Photophysics), after pre-incubation for 10 min at 25°C. Spectra between 200 and 250 nm of 1 μM proteins were measured in Buffer A.

4.7 | ANS fluorescence measurements

ANS fluorescence spectra of the proteins were obtained between 420 and 600 nm with excitation at 395 nm, using a Hitachi F-4500 spectrofluorometer. Spectra of 1 μM proteins were measured in Buffer A or Buffer B in the presence of 150 μM ANS at 25°C in a thermostatted cuvette. ANS binding to 0.4 or 1 μM proteins against ANS concentration were represented as fluorescence intensity at 485 nm after excitation at 390 nm, measured using a Thermo Scientific Fluoroskan® Ascent microplate fluorometer. All of the samples containing ANS were pre-incubated at 25°C for 3 h to reach binding equilibrium before measurements.

4.8 | In vitro amyloid fibril formation

Amyloid fibril formation of HTT exon 1 was performed at 37°C in Buffer A, by cleavage of the GST tag ahead of HTT exon 1 with thrombin on standing for 1–2 days (no high-efficiency thrombin cleavage site is present within the HTT exon 1 sequence), or with shaking at 300 rpm for 3–4 days in an Innova 4230 incubator when there was no GST tag (for 20QPR65/A and 49QPR65/A). In the proteins with GST tag the cleavage sequence of thrombin before the HTT exon 1 is "LVPRGS" and the extra residues are "GS" after thrombin cleavage. The extent of fibril formation was monitored by assay of ThT or ANS binding, as described (Jiang et al., 2004; Zhu et al., 2003; LeVine, 1999; Bolognesi et al., 2010; Bertoncini and Celej, 2011). ThT was dissolved to 10 μM in 50 mM Tris (pH 8.4). At regular time intervals, 10 μL aliquots were removed from the incubated samples and mixed with 600 μL of the ThT solution. ThT fluorescence was measured immediately after addition of the aliquots to the ThT mixture on a Shimadzu RF-5301PC spectrofluorimeter between 460 and 560 nm with an excitation wavelength of 450 nm and slits of 5 nm for both excitation and emission. For each sample, the intensity of ThT fluorescence at 485 nm was measured by averaging the signals over a 10 s period, from which a corresponding blank was subtracted. Fibril seeds were prepared by sonicating mature fibrils, and their concentration was determined according to the protein concentration before fibril formation, as described (Zhang et al., 2010; Fei and Perrett, 2009). Under shaking conditions, fibril seeds were added into the fibril formation system at the beginning. The seed concentration was 10% of the initial concentration of monomeric fibril-forming proteins.

4.9 | Atomic force microscopy

Atomic force microscopy was used to analyze fibril formation of 20Q HTT exon 1, 49Q HTT exon 1, 20QPR65/A and 49QPR65/A over time, and was carried out as described (Jiang et al., 2004; Lian et al., 2007). Samples were imaged at scan sizes of 5 and 10 μm using line scan rates below 2 Hz; 512 × 512 pixels were collected per image. The height of fibrils was measured using the software provided with the instrument.

4.10 | Filter retardation assay

Protein samples of 800 ng applied for filter retardation assay were boiled in buffer containing 2% SDS and 25 mM DTT for 3 min, before they were filtered through a 0.22 μm cellulose acetate membrane using a Biorad Bio-Dot apparatus, as described (Zhang et al., 2010). A polyclonal rabbit anti-PR65/A antibody (1: 20,000 dilution) or a polyclonal goat anti-HTT exon 1 antibody (1:1000 dilution) was employed for immunoblotting of the SDS-resistant aggregates which cannot run through the cellulose acetate membrane. The immunoblot assay was performed as described (Zhang et al., 2010). Anti-HTT exon 1 antibody (Huntingtin (N-18): sc-8767) was from Santa Cruz. Huntingtin (N-18): sc-8767 is an affinity purified goat polyclonal antibody raised against a peptide mapping near the N-terminus of huntingtin of human origin. Anti-PR65/A antibody was produced locally (Beijing 4A Biotech Co., Ltd.) using purified PR65/A as the antigen.

ACKNOWLEDGMENTS

We thank Dr. Huiyong Lian for advice on PCR of CAG repeats, Dr. Zairong Zhang for construction of the PR65/A-pRSETa plasmid, Dr. Li Fei for construction of the U(1-93)PR65/A-pRSETa plasmid, and Dr. Lijun Chen for assistance with the Pistar CD instrument. We also thank Dr. Max Tsytlonok for advice on unfolding and refolding of PR65/A.

FUNDING INFORMATION

This work was supported by the National Natural Science Foundation of China (31920103011, 31770829, 32171443),

the National Laboratory of Biomacromolecules, and the CAS Center of Excellence in Biomacromolecules.

CONFLICT OF INTEREST STATEMENT

The authors declare there is no conflict of interest.

DATA AVAILABILITY STATEMENT

All data are contained within the manuscript.

ORCID

Hong Zhang https://orcid.org/0000-0001-9204-2547
Si Wu https://orcid.org/0000-0001-7743-8236
Laura S. Itzhaki https://orcid.org/0000-0001-6504-2576
Sarah Perrett https://orcid.org/0000-0003-0137-0997

REFERENCES

Andrade MA, Bork P. HEAT repeats in the Huntington's disease protein. Nat Genet. 1995;11:115–6.

Bertoncini CW, Celej MS. Small molecule fluorescent probes for the detection of amyloid self-assembly in vitro and in vivo. Curr Protein Pept Sci. 2011;12:205–20.

Bolognesi B, Kumita JR, Barros TP, Esbjorner EK, Luheshi LM, Crowther DC, et al. ANS binding reveals common features of cytotoxic amyloid species. ACS Chem Biol. 2010;5:735–40.

Bourne PE, Palidwor GA, Shcherbinin S, Huska MR, Rasko T, Stelzl U, et al. Detection of alpha-rod protein repeats using a neural network and application to huntingtin. PLoS Comput Biol. 2009;5:e1000304.

Caterino M, Squillaro T, Montesarchio D, Giordano A, Giancola C, Melone MAB. Huntingtin protein: a new option for fixing the Huntington's disease countdown clock. Neuropharmacology. 2018;135:126–38.

Chen MZ, Mok SA, Ormsby AR, Muchowski PJ, Hatters DM. N-terminal fragments of huntingtin longer than residue 170 form visible aggregates independently to polyglutamine expansion. J Huntingtons Dis. 2017;6:79–91.

Chen M, Wolynes PG. Aggregation landscapes of huntingtin exon 1 protein fragments and the critical repeat length for the onset of Huntington's disease. Proc Natl Acad Sci U S A. 2017;114:4406–11.

Chen Y, Xu Y, Bao Q, Xing Y, Li Z, Lin Z, et al. Structural and biochemical insights into the regulation of protein phosphatase 2A by small t antigen of SV40. Nat Struct Mol Biol. 2007;14:527–34.

Cho US, Xu W. Crystal structure of a protein phosphatase 2A heterotrimeric holoenzyme. Nature. 2007;445:53–7.

Cooper JK, Schilling G, Peters MF, Herring WJ, Sharp AH, Kaminsky Z, et al. Truncated N-terminal fragments of huntingtin with expanded glutamine repeats form nuclear and cytoplasmic aggregates in cell culture. Hum Mol Genet. 1998;7:783–90.

Culver BP, Savas JN, Park SK, Choi JH, Zheng S, Zeitlin SO, et al. Proteomic analysis of wild-type and mutant huntingtin-associated proteins in mouse brains identifies unique interactions and involvement in protein synthesis. J Biol Chem. 2012;287:21599–614.

Dyer RB, McMurray CT. Mutant protein in Huntington disease is resistant to proteolysis in affected brain. Nat Genet. 2001;29:270–8.

Fei L, Perrett S. Disulfide bond formation significantly accelerates the assembly of Ure2p fibrils because of the proximity of a potential amyloid stretch. J Biol Chem. 2009;284:11134–41.

Gatchel JR, Zoghbi HY. Diseases of unstable repeat expansion: mechanisms and common principles. Nat Rev Genet. 2005;6:743–55.

Gill SC, von Hippel PH. Calculation of protein extinction coefficients from amino acid sequence data. Anal Biochem. 1989;182:319–26.

Grinthal A, Adamovic I, Weiner B, Karplus M, Kleckner N. PR65, the HEAT-repeat scaffold of phosphatase PP2A, is an elastic connector that links force and catalysis. Proc Natl Acad Sci U S A. 2010;107:2467–72.

Groves MR, Hanlon N, Turowski P, Hemmings BA, Barford D. The structure of the protein phosphatase 2A PR65/A subunit reveals the conformation of its 15 tandemly repeated HEAT motifs. Cell. 1999;96:99–110.

Guo Q, Bin H, Cheng J, Seefelder M, Engler T, Pfeifer G, et al. The cryo-electron microscopy structure of huntingtin. Nature. 2018;555:117–20.

Hackam AS, Singaraja R, Wellington CL, Metzler M, McCutcheon K, Zhang T, et al. The influence of huntingtin protein size on nuclear localization and cellular toxicity. J Cell Biol. 1998;141:1097–105.

Harding RJ, Loppnau P, Ackloo S, Lemak A, Hutchinson A, Hunt B, et al. Design and characterization of mutant and wild-type huntingtin proteins produced from a toolkit of scalable eukaryotic expression systems. J Biol Chem. 2019;294:6986–7001.

Harjes P, Wanker EE. The hunt for huntingtin function: interaction partners tell many different stories. Trends Biochem Sci. 2003;28:425–33.

Ignatova Z, Gierasch LM. Extended polyglutamine tracts cause aggregation and structural perturbation of an adjacent beta barrel protein. J Biol Chem. 2006;281:12959–67.

Jiang Y, Li H, Zhu L, Zhou JM, Perrett S. Amyloid nucleation and hierarchical assembly of Ure2p fibrils. Role of asparagine/glutamine repeat and nonrepeat regions of the prion domains. J Biol Chem. 2004;279:3361–9.

Jung T, Shin B, Tamo G, Kim H, Vijayvargia R, Leitner A, et al. The polyglutamine expansion at the N-terminal of huntingtin protein modulates the dynamic configuration and phosphorylation of the C-terminal HEAT domain. Structure. 2020;28:1035–1050.e1038.

Kaynak BT, Dahmani ZL, Doruker P, Banerjee A, Yang SH, Gordon R, et al. Cooperative mechanics of PR65 scaffold underlies the allosteric regulation of the phosphatase PP2A. Structure. 2023;31:607–618.e603.

Kim YJ, Sapp E, Cuiffo BG, Sobin L, Yoder J, Kegel KB, et al. Lysosomal proteases are involved in generation of N-terminal huntingtin fragments. Neurobiol Dis. 2006;22:346–56.

Kim YJ, Yi Y, Sapp E, Wang Y, Cuiffo B, Kegel KB, et al. Caspase 3-cleaved N-terminal fragments of wild-type and mutant huntingtin are present in normal and Huntington's disease brains, associate with membranes, and undergo calpain-dependent proteolysis. Proc Natl Acad Sci U S A. 2001;98:12784–9.

Landles C, Sathasivam K, Weiss A, Woodman B, Moffitt H, Finkbeiner S, et al. Proteolysis of mutant huntingtin produces an exon 1 fragment that accumulates as an aggregated protein

in neuronal nuclei in Huntington disease. J Biol Chem. 2010; 285:8808–23.
Lechward K, Awotunde OS, Swiatek W, Muszynska G. Protein phosphatase 2A: variety of forms and diversity of functions. Acta Biochim Pol. 2001;48:921–33.
LeVine H 3rd. Quantification of beta-sheet amyloid fibril structures with thioflavin T. Methods Enzymol. 1999;309:274–84.
Li SH, Li XJ. Aggregation of N-terminal huntingtin is dependent on the length of its glutamine repeats. Hum Mol Genet. 1998;7: 777–82.
Li H, Li SH, Yu ZX, Shelbourne P, Li XJ. Huntingtin aggregate-associated axonal degeneration is an early pathological event in Huntington's disease mice. J Neurosci. 2001;21:8473–81.
Li W, Serpell LC, Carter WJ, Rubinsztein DC, Huntington JA. Expression and characterization of full-length human huntingtin, an elongated HEAT repeat protein. J Biol Chem. 2006;281: 15916–22.
Lian HY, Zhang H, Zhang ZR, Loovers HM, Jones GW, Rowling PJ, et al. Hsp40 interacts directly with the native state of the yeast prion protein Ure2 and inhibits formation of amyloid-like fibrils. J Biol Chem. 2007;282:11931–40.
Marques Sousa C, Humbert S. Huntingtin: here, there, everywhere! J Huntingtons Dis. 2013;2:395–403.
Martindale D, Hackam A, Wieczorek A, Ellerby L, Wellington C, McCutcheon K, et al. Length of huntingtin and its polyglutamine tract influences localization and frequency of intracellular aggregates. Nat Genet. 1998;18:150–4.
Masino L, Kelly G, Leonard K, Trottier Y, Pastore A. Solution structure of polyglutamine tracts in GST-polyglutamine fusion proteins. FEBS Lett. 2002;513:267–72.
Muchowski PJ, Schaffar G, Sittler A, Wanker EE, Hayer-Hartl MK, Hartl FU. Hsp70 and hsp40 chaperones can inhibit self-assembly of polyglutamine proteins into amyloid-like fibrils. Proc Natl Acad Sci U S A. 2000;97:7841–6.
Perrett S, Jones GW. Insights into the mechanism of prion propagation. Curr Opin Struct Biol. 2008;18:52–9.
Perutz MF, Johnson T, Suzuki M, Finch JT. Glutamine repeats as polar zippers: their possible role in inherited neurodegenerative diseases. Proc Natl Acad Sci U S A. 1994;91:5355–8.
Proskura AL, Vechkapova SO, Zapara TA, Ratushniak AS. Protein–protein interactions of huntingtin in the hippocampus. Mol Biol (Mosk). 2017;51:734–42.
Roze E, Bonnet C, Betuing S, Caboche J. Huntington's disease. Adv Exp Med Biol. 2010;685:45–63.
Saudou F, Humbert S. The biology of huntingtin. Neuron. 2016;89: 910–26.
Scherzinger E, Lurz R, Turmaine M, Mangiarini L, Hollenbach B, Hasenbank R, et al. Huntingtin-encoded polyglutamine expansions form amyloid-like protein aggregates in vitro and in vivo. Cell. 1997;90:549–58.
Silva JL, Miles EW, Weber G. Pressure dissociation and conformational drift of the beta dimer of tryptophan synthase. Biochemistry. 1986;25:5780–6.
Tao M, Pandey NK, Barnes R, Han S, Langen R. Structure of membrane-bound huntingtin exon 1 reveals membrane interaction and aggregation mechanisms. Structure. 2019;27:1570–1580.e1574.
Thakur AK, Jayaraman M, Mishra R, Thakur M, Chellgren VM, L Byeon I-J, et al. Polyglutamine disruption of the huntingtin exon 1 N terminus triggers a complex aggregation mechanism. Nat Struct Mol Biol. 2009;16:380–9.
The Huntington's Disease Collaborative Research Group. A novel gene containing a trinucleotide repeat that is expanded and unstable on Huntington's disease chromosomes. Cell. 1993;72:971–83.
Tsytlonok M, Craig PO, Sivertsson E, Serquera D, Perrett S, Best RB, et al. Complex energy landscape of a giant repeat protein. Structure. 2013;21:1954–65.
Wacker JL, Zareie MH, Fong H, Sarikaya M, Muchowski PJ. Hsp70 and Hsp40 attenuate formation of spherical and annular polyglutamine oligomers by partitioning monomer. Nat Struct Mol Biol. 2004;11:1215–22.
Wagner AS, Politi AZ, Ast A, Bravo-Rodriguez K, Baum K, Buntru A, et al. Self-assembly of mutant huntingtin exon-1 fragments into large complex fibrillar structures involves nucleated branching. J Mol Biol. 2018;430:1725–44.
Wang XY, Zhang ZR, Perrett S. Characterization of the activity and folding of the glutathione transferase from Escherichia coli and the roles of residues Cys(10) and His(106). Biochem J. 2009;417:55–64.
Wanker EE, Ast A, Schindler F, Trepte P, Schnoegl S. The pathobiology of perturbed mutant huntingtin protein-protein interactions in Huntington's disease. J Neurochem. 2019;151:507–19.
Warner JB t, Ruff KM, Tan PS, Lemke EA, Pappu RV, Lashuel HA. Monomeric huntingtin exon 1 has similar overall structural features for wild-type and pathological polyglutamine lengths. J Am Chem Soc. 2017;139:14456–69.
Wellington CL, Ellerby LM, Gutekunst CA, Rogers D, Warby S, Graham RK, et al. Caspase cleavage of mutant huntingtin precedes neurodegeneration in Huntington's disease. J Neurosci. 2002;22:7862–72.
Xu Y, Chen Y, Zhang P, Jeffrey PD, Shi Y. Structure of a protein phosphatase 2A holoenzyme: insights into B55-mediated tau dephosphorylation. Mol Cell. 2008;31:873–85.
Yalinca H, Gehin CJC, Oleinikovas V, Lashuel HA, Gervasio FL, Pastore A. The role of post-translational modifications on the energy landscape of huntingtin N-terminus. Front Mol Biosci. 2019;6:95.
Yang H, Yang S, Jing L, Huang L, Chen L, Zhao X, et al. Truncation of mutant huntingtin in knock-in mice demonstrates exon1 huntingtin is a key pathogenic form. Nat Commun. 2020;11: 2582.
Zhang H, Xu LQ, Perrett S. Studying the effects of chaperones on amyloid fibril formation. Methods. 2010;53:285–94.
Zhu L, Zhang XJ, Wang LY, Zhou JM, Perrett S. Relationship between stability of folding intermediates and amyloid formation for the yeast prion Ure2p: a quantitative analysis of the effects of pH and buffer system. J Mol Biol. 2003;328:235–54.

How to cite this article: Zhang H, Wu S, Itzhaki LS, Perrett S. Interaction between huntingtin exon 1 and HEAT repeat structure probed by chimeric model proteins. Protein Science. 2023;32(12):e4810. https://doi.org/10.1002/pro.4810